

The dispersed infrared background in WFC3 G102 and G141 observations

N. Pirzkal, R. Ryan

April 16, 2020

ABSTRACT

Background removal is one of the, if not the most, important step during the extraction and calibration of slitless observations. Any error in the amount of dispersed background light has an immediate effect on the quality of the extracted spectra. We show in this work how we determined three new independent background components (Zodi background, HeI emission, and “Scatter” Earth light) which have different spectral signature and therefore contribute differently to the overall background of the final observation. We also introduce a generalized implementation of the variable background subtraction described in ISR 2017-01. This approach allows us to account for a temporal variation of both the HeI and “Scatter” light and retain the use of on-the-ramp fitting in CALWF3. We also investigate, using all of the available G102 and G141 archival data, the conditions under which we measure an increased levels of HeI and “scatter” light emission.

1. The dispersed background

While the majority of G102 and G141 observations can be seen to have background levels that vary, most of them appear to have the same background structure. This points to the fact that the principle source of background in WFC3 IR slitless observations is due to

Zodiacal light. The Zodiacal background varies in intensity as a function of position on the sky and as a function of time of the year but the Zodiacal spectrum varies only moderately at the wavelengths covered by G102 and G141. Figure 1 shows models of the Zodi and Galactic backgrounds at two different positions on the sky and at two different dates. As a result, we can subtract the dispersed 2D background from many slitless observations by simply scaling and subtracting a model of the dispersed Zodiacal background component. There is however a subset of WFC3 IR slitless observations for which the same Zodiacal light background is a poor fit. This was identified several years ago in direct imaging (WFC3 ISR 2014-03) and led to the effort to create a dispersed grism model of this component (WFC3 ISR 2015-17) which was identified as HeI glow from the Earth atmosphere. We also determined that, due to the changing limb angle between the Earth’s atmosphere and HST, the amount of HeI light varies during the course of an exposure (WFC3 ISR 2017-05). We show examples of a Zodiacal light dominated G102 observation as well as a HeI light dominated one in Figure 2. We also show a row average (after masking spectra) of these two images in Figure 2 to demonstrate why scaling of a Zodiacal light component does not work to correct for a dispersed HeI background. In practice, many observations suffer from a varying ratio of Zodiacal light and HeI light. A method to estimate the amount of Zodiacal and HeI background in a dataset was described in WFC3 ISR 2015-17 but this method did not account for a time variation in the make up of the background while the exposures were taken.

2. Newly Available Data

An increased number of G102 and G141 WFC3 observations have been accumulating in the archive as time goes on. For this reason, we initiated a project to create updated versions of the master G102 and G141 sky backgrounds. Previous versions of the G102 and G141 background models are now several years old (WFC3 ISR 2015-17) and have a few undesired issues: 1) Relatively low signal-to-noise 2) Imprints of the IR Blobs 3) limited to two components 4) Residual artifacts, especially in the HeI components. The Blobs are clearly visible in Zodi components in Figures 3 to 6 in WFC3 ISR 2015-17. In this ISR, we selected data differently for the processes of determining the Zodi components and any time-varying component and this is described in more detail in Sections 3.2, 4.1, and 5.1.

2.1. Use of Flat-fielding

WFC3 grism observations are not flat-fielded by default, and the only flat-fielding that takes place while running CALWF3 is the use of a special flat-field that only applies the

quadrant specific gain values. G102 and G141 observations however have a lot of structure and artifacts (such as the “wagon wheel” at the bottom right corner, visible in Figure 4). The use of a broad imaging flat-field is helpful to mitigate the effect of these artifacts on the statistics we derive for individual images. However, the current broad band flat-fields are not ideal for this because they are affected by the IR Blobs (WFC3 2012-15). The Blobs are caused by deposits on the pick off mirror and therefore do not result in round blobs in dispersed images, but rather appear as elongated deficits of light in the background. We opted to flat-field our observations with a custom F105W (F140W) flat-field when analyzing G102 (G141) observations. These flat-fields are early releases of on-orbit flat-fields which were created in a manner similar to what was done in WFC3 2011-11, but they were constructed from significantly more data and therefore with a higher signal-to-noise. We took care to identify and replace areas affected by the IR Blobs with a smooth version of the flat-field. Figure 3 shows the flat-fields we have used and how they differ cosmetically from the current broad band filters. The results of applying this broad band filter flat to a grism observation is shown in Figure 5, where we show the same observations as in Figure 4 after we apply this flat-field. The use of a flat-field while creating the models of the dispersed background will result in components that have been flat-fielded and can be used to subtract the background from similarly flat-fielded observations. Likewise, the flat-fielding of the background models can be subsequently removed from our models if one wishes to continue to work on non-flat-fielded grism observations.

3. Zodi background components

3.1. Masking spectra

As we are interested in modeling the dispersed Zodi sky background in observations, we started by creating individual masks for each dataset to mask out astronomical sources. Masks were created using the FLT product for each of our datasets using the `photutils` Python package. We found, empirically, that we were able to mask out dispersed spectra using a simple 16x16 pixel 2D kernel generated by repeating a very narrow (FWHM=0.25 pixels) 1D Gaussian profile along the x-direction. This kernel was used with the `photutils.background.Background2D` function with a background box size of 169 pixels. The resulting estimate of the 2D background was subtracted from the original data. An aggressive detection threshold of one tenth of the FLT error array values, and a minimum of 50 connected pixels were then used with the `photutils.detect_sources` to detect all dispersed spectra. Figure 6 shows a G141 observations, the initial 2D continuum estimate, and the final mask for this observation. Masks such as this one were used to mask all sources

in individual IMSET in all of the steps we describe below.

3.2. Zodi Data

The Zodi component, which is assumed to not vary during the course of an exposure, was generated by combining as many masked IMSETs as possible. We started by first identifying G102 and G141 observations with exposure times longer than 200s and devoid of large, extended or diffused sources. As shown in Table 1, we identified, as of February 2019, 19 G102 proposals and 30 G141 proposals for a total of 3467 and 3091 datasets, using the G102 and G141 grisms, respectively. The number of individual reads, since WFC3 data are non-destructively read (IMSET) several times during an exposures are 44334 and 37896 in G102 and G141, respectively. This is a significant increase of 56% (30%) in the number of datasets in the pool of data we can use to model the dispersed background of G102 (G141). As we wanted to avoid any source of variability at this stage, we looked for a gradual rise, or decrease, in the average background levels in successive IMSETS and only retain data when the background remained constant to within 0.005 e-/s of the minimum observed background level, minimum established by the first 4 IMSETS or the last 4 IMSETS of an observations. Figure 7 shows how we identified which IMSETs could be used and combined to generate the Zodi background components. We applied this selection method to all available observations and thus select a sample of individual IMSETs that are most likely to have a dispersed background made up solely of dispersed Zodiacal light. These individual masked datasets were normalized to unity in the region [550:900,550:900], avoiding bad pixels flagged in the DQ array and all the masked pixels. We conservatively avoided any pixel with a DQ value bit set, except for the Blob DQ bit (512 in decimal) since these are relevant only for imaging data. Final Zodiacal light components for G102 and G141 were created by combining these data together. A total of 3063 G102 and 3549 G141 masked IMSETs were used to produce the final G102 and G141 Zodiacal background models.

3.3. Generating Zodi components

Estimates of the Zodi components were assembled by combining all of the masked data identified as we described above. We used a 4 sigma clipped median algorithm, excluding pixels with a value lower than -1 or higher than +3. A first estimate of the background signal was computed. The process was then repeated using this initial estimate to scale each individual masked dataset before combining them. The Zodi component is shown in the left panel of Figure 9.

Filter	Proposals	Number of datasets	Scaling IMSETs
<i>G102</i>	11359 11696 12190, 12283 12461 12558 12568 12685 12786 12902 12927 13352 13399 13517 13779 13839 14178 14227 15163	3467	44334
<i>G141</i>	11359 11600 11696 1209 12177 12190 12283 12328 12461 12471 12547 12558 12568 12685 12902 12927 13063 13352 13399 13482 13517 13785 13845 13871 14178 14200 14495 14594 15077 15163	3091	37895

Table 1: *Proposals used in this ISR to model the Zodi background for each of the IR grisms. We also list the number of IMSETs (readout) in the associated IMA files.*

4. HeI background components

4.1. HeI Data

The amount of glow from the HeI line from the Earth’s upper atmosphere varies as HST is pointed closer to the Earth Limb. It is a significant effect and leads to a large increase in the dispersed background at either the beginning or end of observations. As seen in Figure 7, the variation in this dispersed background can be quite large and in this example ranges from $0.0\ e^-/s$ to $\approx 0.8e^-/s$. Fortunately, WFC3 IR observations are made up of multiple reads during a given exposure. Since the astronomical objects do not typically vary during the course of a few hundred seconds exposure, we can expect significant, non zero, residuals when subtracting one IMSET from another IMSET to be due to some variation in the background. In the rest of this document, we refer to these differential IMSETs as DIMSETs. Since DIMSETs should only contain the signal that varies between two IMSETs, any constant signal caused by the sources or Zodi light should in principle be removed and we should only be left with whatever dispersed background has been varying. In practice, there are sometimes small issues with tracking during the course of an observation, as well as persistence, that can cause astronomical sources to not subtract cleanly. This is particularly

true when observations are taken while WFC3 is not being used as the prime instrument and the velocity aberration correction that is computed is for another instrument (ISR OSG-CAL-97-06).

We therefore did not restrict ourselves to data obtained as part of the proposals listed in Table 1 and instead examined every G102 and G141 datasets in MAST obtained while WFC3 was the prime instrument and computed all possible DIMSETs for each of these observations. As on-the-ramp fitting is not applied to IMA files, we computed every pair differences between successive IMA reads. This essentially increased our number of samplings. As cosmic rays and satellite trails appear in these DIMSETs (as they are transient effects), we generate masks for them as we did when examining the Zodi dominated datasets. These masks however contain a significantly small number of masked pixels since the dispersed signal from astronomical sources is generally well removed. Having some a-priori knowledge of the general shapes of both G102 and G141 HeI dispersed components, we examined and retained only DIMSETs that showed similar levels on the left and right sides of the images. More specifically, we compute the median of the regions between columns 150 and 400 as well as between columns 650 and 900 and retained only DIMSETs where the two differed by less than $0.0075 e^-/s$ while the overall level of the full DIMSETs was greater than $0.1 e^-/s$ (i.e. we had a significant detection of a varying background). The final number of DIMSETs we thus generated was 20255 (from 2479 initial IMA files) for G102 and 12577 (from 3561 initial IMA files) for G141. (3838 G102 observations and 34221 G141 observations).

4.2. Generating HeI components

The HeI dominated DIMSETs were normalized and combined using the same two-step method we used to create our Zodiacal light background components in Section 3. The HeI component is shown in the middle panel of Figure 9.

5. “Scattered” light background components

5.1. “Scatter” Data

During the course of generating the HeI background components, we identified a small fraction of the exposures that showed a completely different illumination pattern than the previously described Zodi and HeI components. This is shown in Figure 8. This pattern could not be reproduced using solely a combination of Zodiacal and HeI dispersed components and affects only the left hand side of image. Using a Zodiacal/HeI combination leads to the

left most part of the data to be poorly subtracted, leaving residuals larger than $0.1e^-/s$. Observers have traditionally simply row averaged these residuals, fit them and removed them as an extra background subtraction step (See Pirzkal et al. 2017 for an example). This method does reduce the residuals of the masked medianed detector rows, but it fails to deal with the 2D structure of this excess light and any variation as a function of detector row. We therefore modelled this component separately. While we do not know at this time the exact cause of this illumination, we refer to it as the Scattered light component. This is not to imply that we understand the source of this light but simply that there is at least one extra recurring contributor to the overall grism background. Since this light seems to produce a similar dispersed background, it implies that the spectrum of this light remains constant. The main reason for isolating this component is to ensure that our estimates of the HeI backgrounds would not be biased by it, especially in the regions where the HeI and this component are most different, i.e. the left side of the detector. We re-examined all of the data described in 5.2 and identified DIMSETS that were rejected as being HeI dominated, mostly because they violated the HeI test that the left and right sides of a DIMSET should have similar levels, and we retained all DIMSETs where the the regions between columns 100 to 400 had a median level that is $0.05 e^-/s$ higher than the median level between columns 550 to 850. We identified 560 DIMSETs for G102 and 1717 for G141.

We therefore proceeded to estimate this additional component by re-examining all of the DIMSETs from Section 5.2, scaling and subtracting our newest estimate of the HeI dispersed background, and looked for cases where a significant signal remained. The scaling process was performed only using the right hand side of the image as we could see that the additional signal affects the left half of the detector only. We retained all DIMSETs where an average residual greater than $0.05e^-/s$ was detected in the HeI subtracted DIMSET. The final versions of the Scattered background component were generated by combining 534 and 444 DIMSETs for G102 and G141, respectively.

5.2. Generating Scattered component

The Scatter dominated DIMSETS were normalized and combined using the same two-step method we used to create our Zodiacal light background components in Section 3. The resulting Scatter light component is shown on the right panel of Figure 9.

6. Additional cleaning and artifact removal

The background components shown in Figure 9 contain noise spikes and other lower level artifacts that are best removed before trying to scale and subtract these models from observations. We therefore further cleaned these background models. As we were interested in removing pixels with wild fluctuations, we examined each column of each model individually and use the generalized Extreme Studentized Deviate test to identified outlier pixels. These pixels were masked and their values replaced with a smooth polynomial fit to the rest of the column values (“scrubbed” models). As these models are meant to be flat-fielded and, assuming that the flat-fielding accounts for individual pixel sensitivity variation, we further smoothed the data using the edge-preserving method from `skimage.restoration`’s `denoise_tv_chambolle`. These “superscrubbed” models are shown in Figure 10. In Figure 11, we show the horizontal cuts of the G102 and G141 components to illustrate the difference in noise levels in the three versions of the background models.

7. New versus old models

Our new Zodiactal, HeI, and Scattered light models for the G102 and G141 grisms are shown in Figures 9 and 10. Qualitatively the new models are similar to what was made available to users previously, but they have subtly different structures. Moreover, the impact of “Blob” and other artifact have been significantly reduced. We show the median rows of our new Zodi and HeI models as well as the previous models in Figures 12 and 13.

8. Using Multiple Background Components

As was discussed in WFC ISR 2014-03, in the case of WFC3 IR imaging and WFC3 ISR 2017-5 for WFC3 IR grism data, when facing the possibility of a background that varies during the observation, one could simply resort to a simple “last minus first” approach. This approach is simple and fast, since it involves subtracting a simple linear combination of the Zodi, HeI, and Scatter components to minimize the background residuals in the final FLT file. However this approach does not take full advantage of the multiple independent detector reads, which can be analyzed separately to lead to an increase in the signal-to-noise of the final FLT. which can lead to an increase in the signal-to-noise of the final FLT. It also does not deal with cosmic ray, thus allowing them to impact the final FLT file. This is what motivated us in ISR 2017-05 to describe an approach by which the HeI level is estimated and subtracted from each individual IMSET of an observation at the IMA file level. This

corrected IMA file can then be processed normally using CALWF3, which applies on-the-ramp fitting to produce a final FLT file. The remaining Zodi background in this FLT file can be estimated and subtracted as a final step. We have implemented a version of this algorithm which solves for a constant Zodi level as well as time varying HeI and Scatter light components. To summarize the process, the problem is posed as the total background in a pixel p of an IMSET i as being the weighted sum of the Zodi (\mathcal{Z}), HeI (\mathcal{B}), and Scatter components (\mathcal{E}):

$$\mathcal{S}_{p,i} = z\mathcal{Z}_p + b_i\mathcal{B}_p + e_i\mathcal{E}_p \quad (1)$$

where z , b_i , and e_i are the level of Zodi, HeI, and Scatter in IMSET i . These quantities can be determined by simply minimizing the residuals between the IMSETs and our compound background model:

$$\chi^2 = \sum_p \sum_i \mathcal{W}_{p,i} (\mathcal{F}_{p,i} - \mathcal{S}_{p,i})^2 \quad (2)$$

and this can be posed as a simple least-square problem

$$\mathbf{v} = \mathbf{M}\mathbf{x} \quad (3)$$

where we want to solve for

$$\mathbf{x} = \{\mathbf{b}, \mathbf{e}, z\} \quad (4)$$

where \mathbf{b} and \mathbf{e} are vectors with as many elements as we have IMSETs. Hence, in the case of two observations taken during a single visit, each with 12 IMSETs, we will solve for one value of z (Zodi), and two 24 elements vectors \mathbf{b} (HeI) and \mathbf{e} (Scatter). The matrix elements of \mathbf{M} and \mathbf{v} are

$$M_{i,i} = \sum_p \mathcal{W}_{p,i} \mathcal{B}_p \mathcal{B}_p \quad (5)$$

$$M_{i,2n} = \sum_p \mathcal{W}_{p,i} \mathcal{Z}_p \mathcal{B}_p \quad (6)$$

$$M_{2n,2n} = \sum_p \sum_i \mathcal{W}_{p,i} \mathcal{Z}_p \mathcal{Z}_p \quad (7)$$

$$M_{n+i,n+i} = \sum_p \mathcal{W}_{p,i} \mathcal{E}_p \mathcal{E}_p \quad (8)$$

$$M_{i,n+i} = \sum_p \mathcal{W}_{p,i} \mathcal{B}_p \mathcal{E}_p \quad (9)$$

$$M_{n+i,2n} = \sum_p \mathcal{W}_{p,i} \mathcal{Z}_p \mathcal{E}_p \quad (10)$$

$$M_{n+i,i} = M_{i,n+i} \quad (11)$$

$$M_{2n+i,i} = M_{i,2n+i} \quad (12)$$

$$v_i = \sum_p \mathcal{W}_{p,i} \mathcal{B}_p \mathcal{F}_{p,i} \quad (13)$$

$$v_{2n} = \sum_p \sum_i \mathcal{W}_{p,i} \mathcal{Z}_p \mathcal{F}_{p,i} \quad (14)$$

$$v_{n+i} = \sum_p \mathcal{W}_{p,i} \mathcal{E}_p \mathcal{F}_{p,i} \quad (15)$$

and \mathbf{x} can be estimated as: $\mathbf{x} = \mathbf{M}^{-1}\mathbf{v}$, which can be performed using a least square algorithm such as the one from `scipy.optimize.lsqr_linear`, or `scipy.optimize.nnls` if ones wants to require that all values of z , \mathbf{b} and \mathbf{e} be positive. The WFC3 team has released a Python implementation of this approach as part of the WFC3TOOLS packages (<https://wfc3tools.readthedocs.io/en/latest/>). The software includes all of the background models we present here as well as the flat-fields shown in Figure 3, which were used to construct the new background models. Users are referred to the WFC3TOOLS package documentation for the different options available when applying the new background models to observations.

9. Background subtraction of archival G102 and G141 data

9.1. Residuals of the WFC3 IR Background Subtraction

Subtraction of the background in grism data using a combination of Zodi, HeI, and Scatter light is not trivial as it strongly depends on our ability to mask (or model) sources. It also fundamentally relies on a lack of any large, diffuse dispersed signal, as well as a lack of unmasked artifacts such as satellite trail. Here we show the results of applying the older background models to some archival observation and compare the results to those obtained when applying the “superscrubbed” versions of our new models. We show in Figures 14 and 15 the average background residuals using the new models and the background residuals when using the older models for several hundreds observations. These plots show the datasets for which the best background subtraction was achieved. We determined the quality of the background subtraction by applying the object masks created during the background subtraction process and compute the row median of the masked images. We then simply added the absolute value of the median row to generate a simple metric that indicates how far from perfect (i.e. 0) the result of the background subtraction was. A value less than $4 \text{ e}^-/\text{s}$ (which is an average residual of $4/1014$, or $0.004 \text{ e}^-/\text{s}$ per pixel is considered to be

good in this context and this selected approximately half of the entire sample of G102 and G141 from the archive. As these Figures demonstrate, the new background models result in overall better background subtraction with slightly lower residuals (as shown by histograms on the right of these figures) and lower systematic errors, especially on the left hand-side of the detector (first 100-200 columns).

9.2. The measured HeI and "Scatter" levels in G102 and G141 Observations

We can apply the method described in Section 8 together with our new Zodi, HeI, and "Scatter" models in an attempt to determine under what circumstances observations are affected by large amount of variable HeI and/or "Scatter" emission. In Figure 16 we show the distribution of Zodi light levels in G102 and G141, which have a median of 0.48 and 1.04 e^-/s , respectively, and are known to depend primarily on the Sun angle (the angle between the Sun and the direction HST is pointing, see WFC3 ISR 2014-11). In Figure 17 we show the distribution of HeI and "scatter" levels. This Figure shows how approximately 47% of the G102 and G141 DIMSETs we examined were affected by more than 0.05 e^-/s HeI emission, about 28000 of 59000 DIMSETs, and with levels as high as 3 e^-/s . The number of DIMSETs affected by "scatter" light is significantly smaller with only about 1% of the DIMSETs (560 out of 59000) affected at a level greater than 0.05 e^-/s but the "scatter" levels that can be as high as what we measured for HeI emission. We examined the actual pointing of HST during these observations to attempt to identify the circumstances under which HeI or "Scatter" emission can be high. As previously shown in WFC3-2015-17, the HeI emission levels are known to be correlated with HST not being in Earth's shadow as the telescope is more likely to be affected by light from the bright Earth limb. While the information about whether HST is in Earth's shadow is available in the JIT file, we used the available HST orbital information and the satellite tracking and orbital prediction program Predict (<https://www.qsl.net/kd2bd/predict.html>) to get a better understanding of where HST was pointing with respect to the Earth during a particular WFC3 observation. Figures 18 to 21 show this information for particular grism observations. In these Figures, we show when HST is in Earth's shadow (green), bright Earth (red), and an intermediate state (orange). We also show the limb angle of the telescope (black), when the observation was taken, as well as the HeI and "scatter" emission levels during each of the DIMSETs (Top panels). As these figures demonstrate, higher levels of HeI occur when HST is not in Earth's shadow and is aiming more closely to the Earth limb (Earth Limb Angle).

The relation between HeI levels and Earth limb angle while above the bright Earth is plotted in Figure 22 and this Figure shows how data taken while pointing closer to the

Earth limb have increased levels of HeI emission (Shown in orange), while data taken while in the Earth’s shadow remain unaffected, even down to low Earth limb angles (Shown in blue). However, this Figure also shows how many observations taken while not in Earth’s shadow are not affected by a large amount of HeI emission. We find that only about 10% of the observations taken while not in Earth’s shadow have HeI levels greater than $0.05\ e^-/s$. The amount of HeI affecting observations taken at low bright Earth limb angles is therefore difficult to pre-determine and it is best to avoid doing so if low background levels are important (This was already noted in past WFC3 ISRs).

If we similarly examine the conditions under which we measure a significant amount of “scatter”, and as we show in Figure 23, we see that “scatter” is detected while HST points in a direction that is close to the bright Earth limb and that “scatter” emission only occurs when the Earth limb angle is below 30 degrees. We find that are under these conditions, 16% of the observations are affected. We found no other correlation between the position of the Sun (aside from the fact that it is the cause of the bright Earth limb), Moon, or the V3 roll angle of HST however. This points to the “scatter” component to also be caused by the Earth or its atmosphere, as are the HeI levels.

Conclusion

We used archival data of G102 and G141 observations to derive new dispersed background models of the Zodi and HeI components for both the G102 and G141 grisms. We identified and generated models of an additional Scattered component which was detected in a small fraction of the observations. We introduced a generalized background subtraction approach that allows for observations to be affected by a varying level of HeI and Scattered light while preserving the ability to run CALWF3 and on-the-ramp fitting to maximize the signal-to-noise of these observations. An implementation of this approach has been incorporated into the WFC3TOOLS python distribution. Comparing these new background models to those that have been available, we find that the new models result in better background subtraction with significantly less variation over the field of view, in particular on the left hand-side of the detector. We showed that while HST is pointing closer to the bright Earth limb, the chance of getting a significant amount of HeI increases. Similarly, we showed how what seems to be Earth based “scatter” light can significantly affect observations taken within 30 degrees of the bright Earth limb. Users can avoid strong HeI and “scatter” contamination in their grism observations by ensuring that their grism observations are taken while in Earth’s shadow and well off from the bright Earth limb. Since imaging is often required to be taken in the same visits as G102 or G141 observations, it is recommended that

imaging be placed at the beginning and end of a visit so that any variation in background levels only affect the imaging part of their program.

10. Acknowledgments

We would like to thank Jay Anderson for his review of this document as well as Ben Sunnquist, Jennifer Mack, and Heather Kurtz for supporting with effort with updated bad pixel maps and flat-fields.

References

- Cox, C. 1997, *Velocity Aberration Correction for Parallel Observation*, ISR OSG-CAL-97-06
- Pirzkal N., Viana A., Rajan A. *The WFC3 “Blobs”*, ISR 2010-06
- Pirzkal N., Mack J., Dahlen T., Sabbi E. *Sky Flats: Generating Improved WFC3 IR Flat-fields*, ISR WFC3 2011-11
- Pirzkal N., Hilbert B. *The WFC3 IR “Blobs” Monitoring*, ISR 2012-15
- Pirzkal N. *The Near Infrared Sky Background*, WFC3-2014-11
- Brammer G., Ryan R., Pirzkal N., *Source-dependent master sky images for the WFC3/IR grisms*, WFC3-2015-17
- Brammer, G., *Reprocessing WFC3/IR Exposures Affected by Time-Variable Backgrounds*, WFC3-2016-16
- Pirzkal N. et al. 2017, *FIGS—Faint Infrared Grism Survey: Description and Data Reduction*, ApJ, 846, 84P
- Pirzkal N., Ryan R. 2017, *Variable He I emission in grism data*, ISR WFC3 2017-05

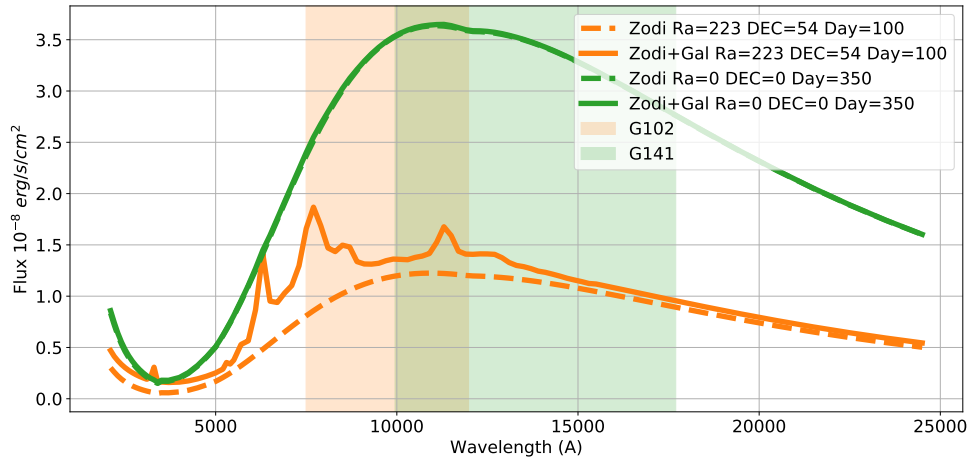


Fig. 1.— Prediction of the background from the Zodi (Dashed lines) and from the Zodi+Galactic background (Solid lines), as generated by the JWST ETC. We also show the approximate bandpasses of the G102 and G141 grisms. While we expect variations in the IR background spectrum as a function of position and time of the year, once accounting for a scaling factor the variations remain at the sub 1% level or so.

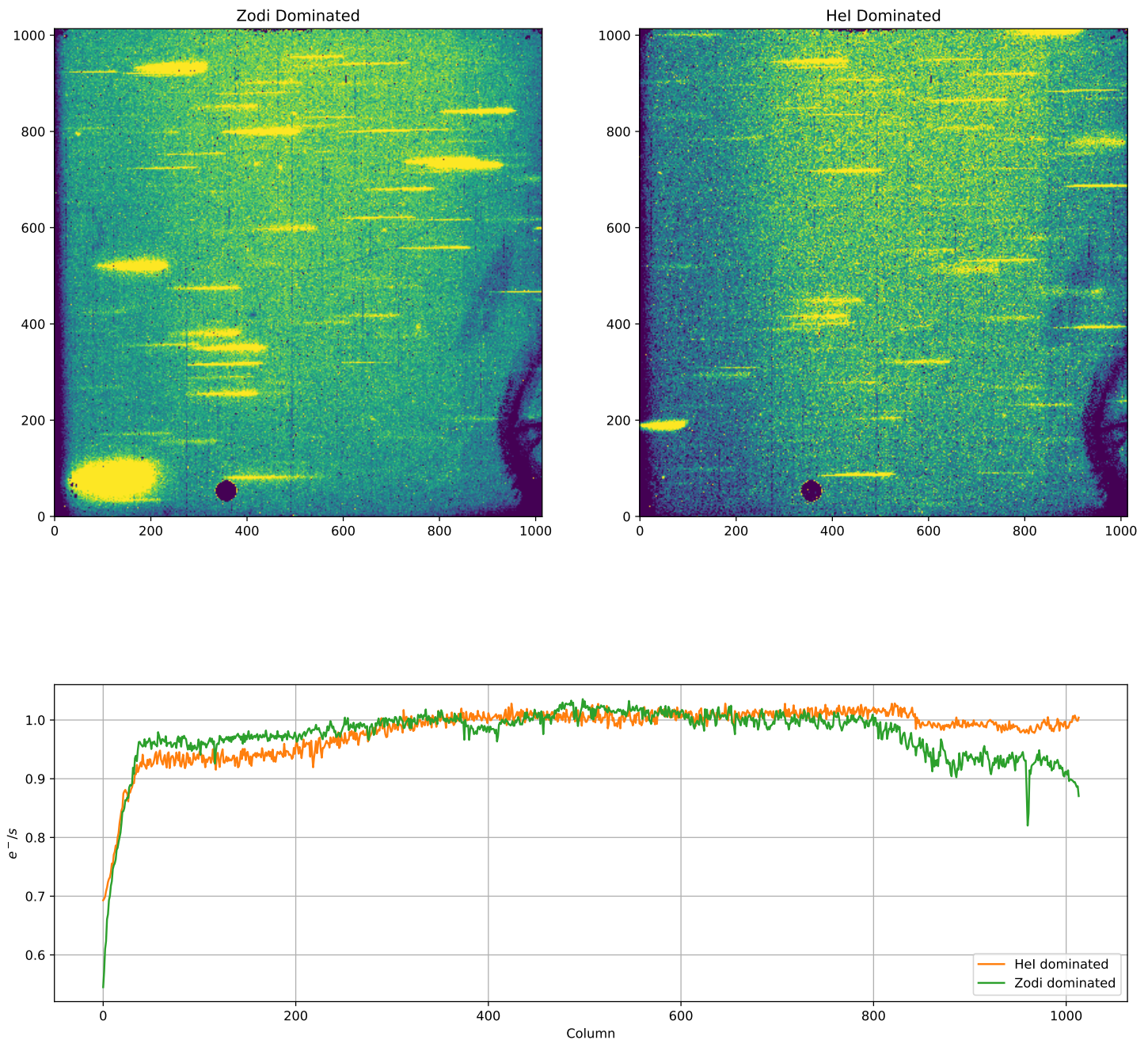


Fig. 2.— Top Left: A G102 observations dominated by Zodiacal light. Top Right: A G102 observation dominated by HeI light. Both images were scaled so that the region spanning the columns 600 to 800 have a median flux of $1 e^-/s$. While it is difficult to see that the left hand side of the Zodiacal light dominated image than the same region on the HeI dominated exposure, the bottom plot shows how their profiles (median row averages after the sources were masked) are different.

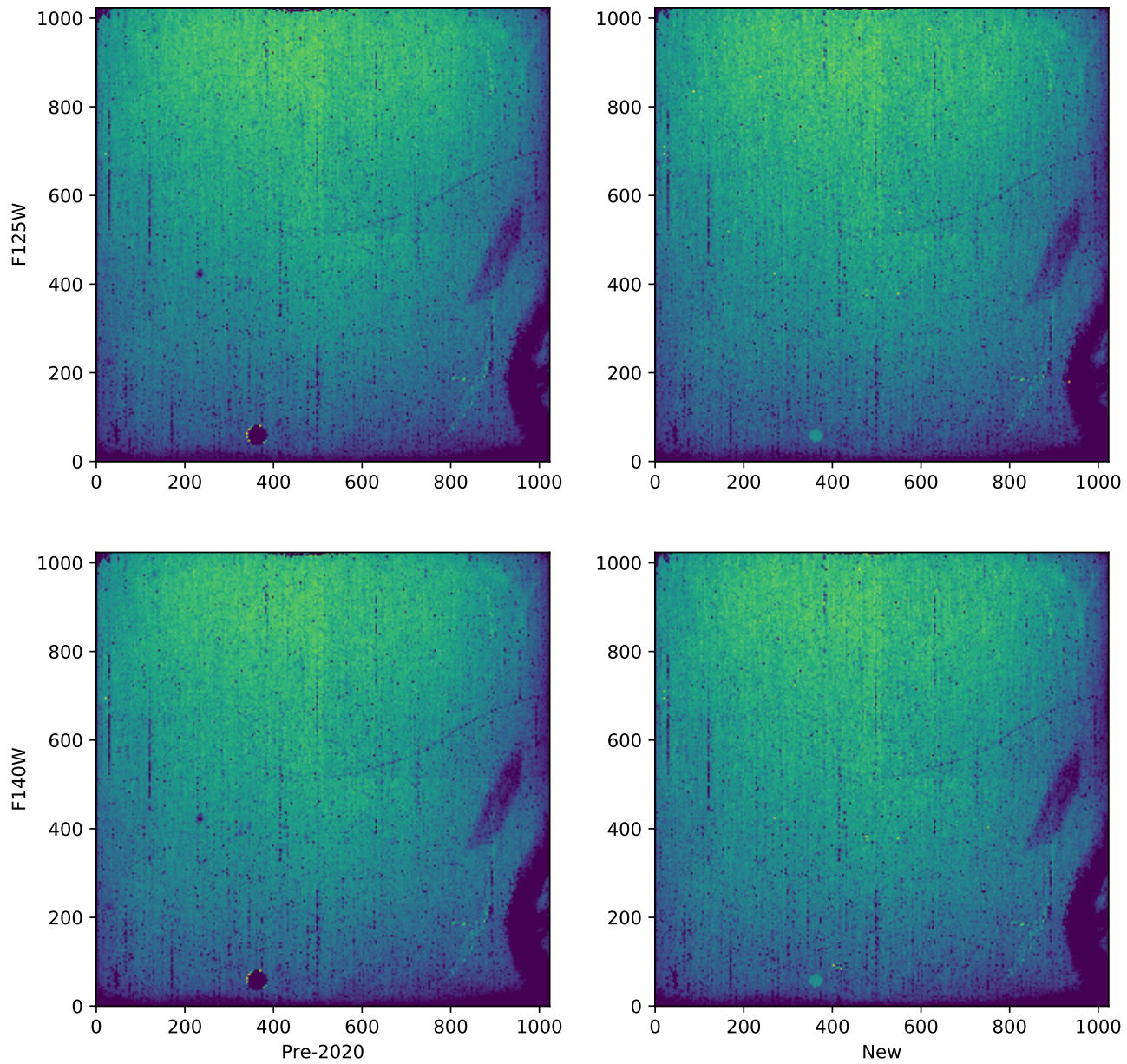


Fig. 3.— The current pipeline flat-fields used for the F105W (top row, left) and F140W (bottom row, left) filters. The improved flat-fields were used, which are devoid of IR Blobs, are shown on the right.

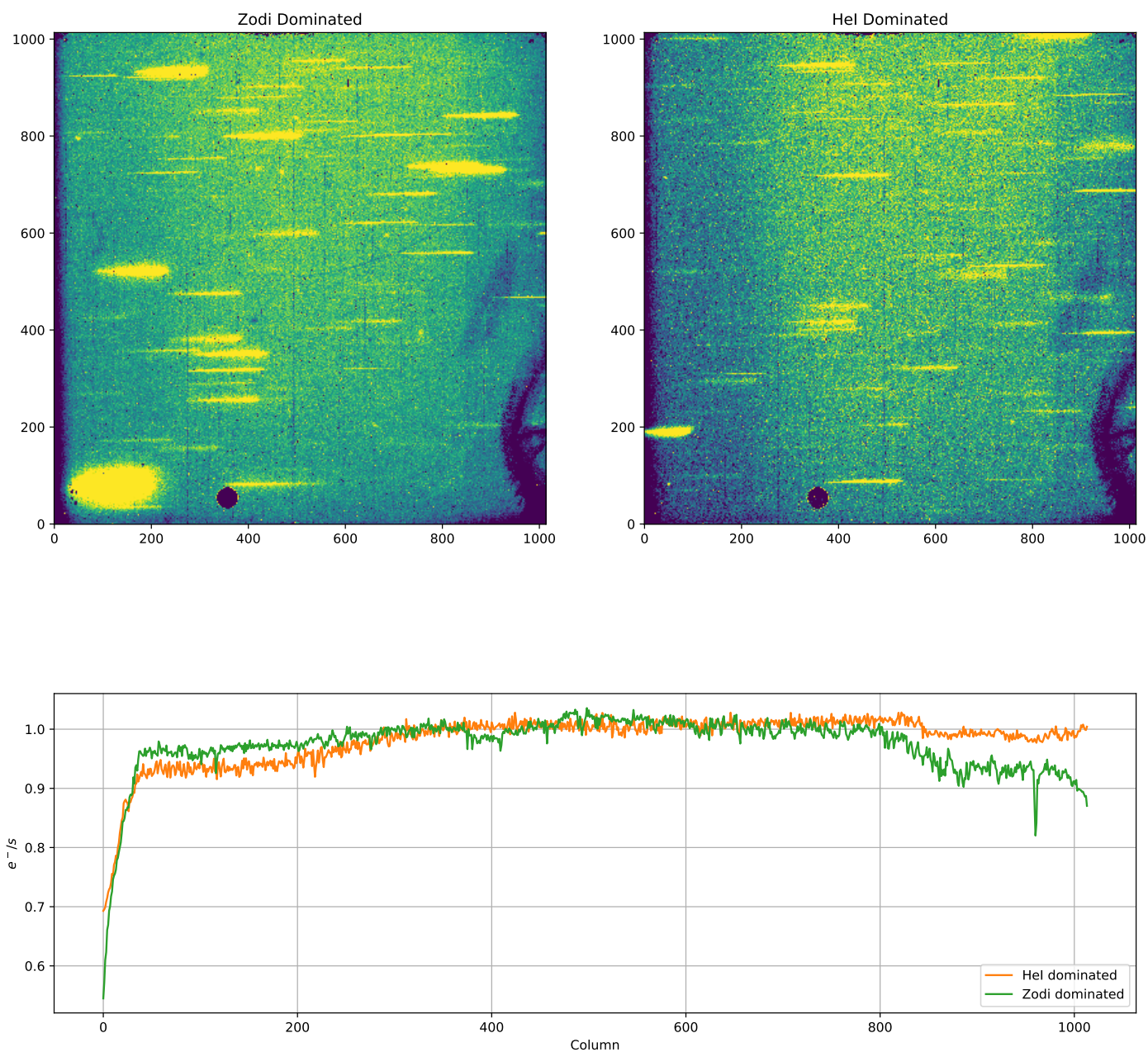


Fig. 4.— Example of Zodi and HeI light dominated G102 observations

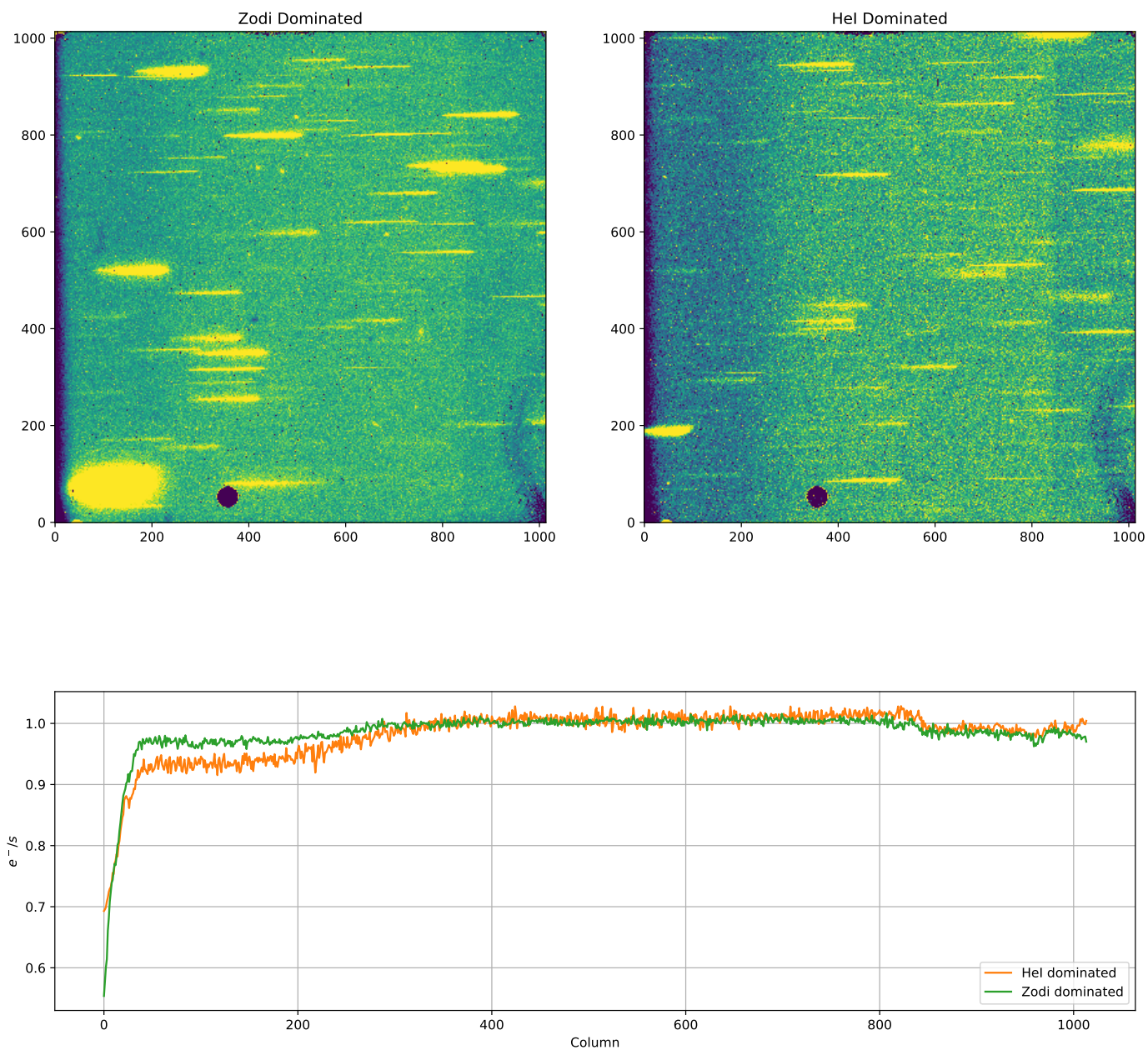


Fig. 5.— Same as Figure 4 but we have applied the flat-fields from the right column of Figure 3 to the observations.

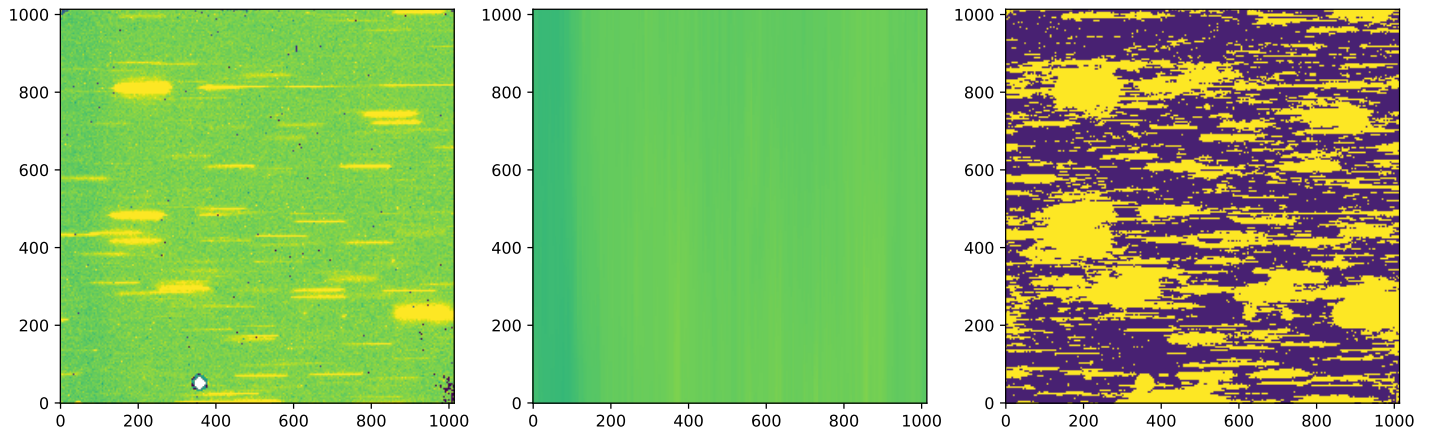


Fig. 6.— A typical WFC3 G141 dataset (left), the `photutils` 2D background estimate which was generated for the sole purpose of detecting dispersed sources (middle), and the mask we generated for this exposure (right). Note that, as shown here, the masks we generated were purposefully aggressive and masked out upwards of 50% of the pixels in each dataset.

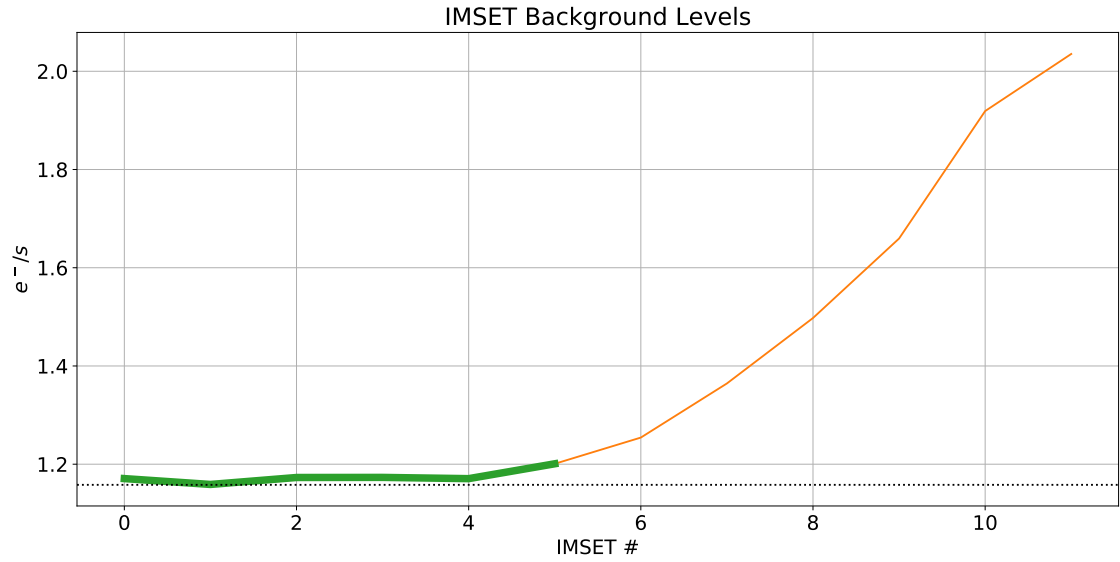


Fig. 7.— Observed mean background level in a typical G141 observation, plotted as a function of DIMSET. The minimum observed value in this case was $1.158 \text{ e}^-/\text{s}$ and the first five DIMSETs (green) are retained in this case.

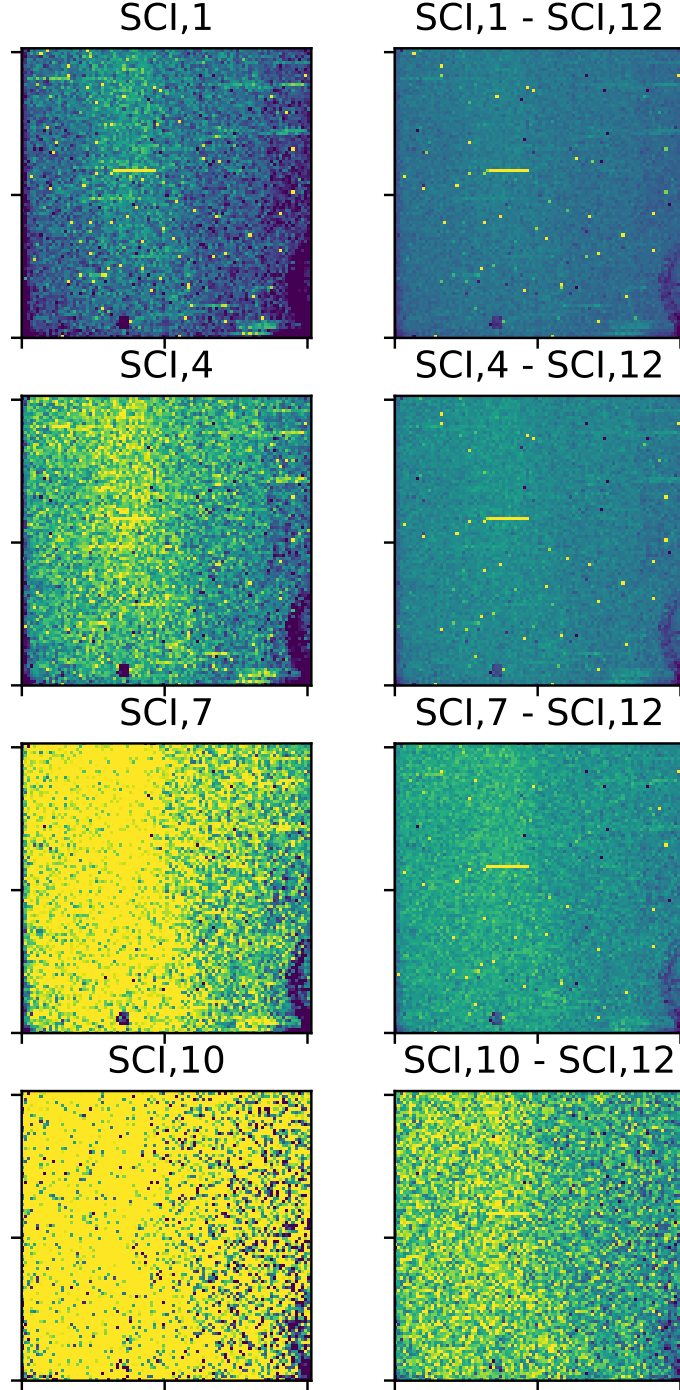


Fig. 8.— Example of a G102 dataset (idnco6opq) that was found to be affected by a non HeI-like, illumination that decreased as a function of exposure time (bottom to top in this Figure). We show the (flat-fielded) IMSET for several non-dststructive reads on the left and the difference between specific IMSETs and the final IMSET on the right (in units of e^-/s). The first few reads are clearly contaminated by extra light on the left side of the image.

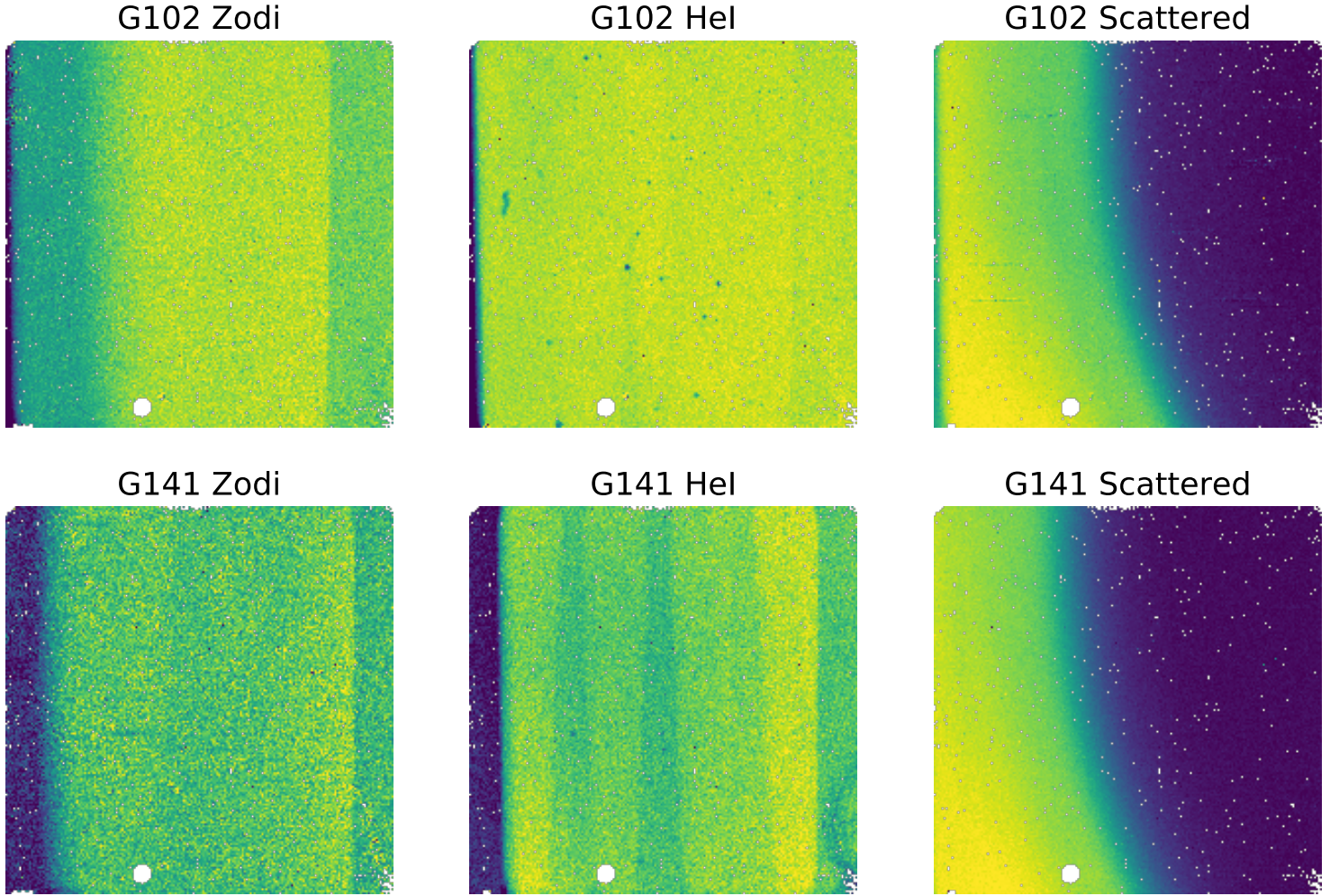


Fig. 9.— The initial G102 and G141 dispersed background estimates derived as part of this study. The effect of the IR Blobs are clearly visible in the Zodiacal light model as they occult the incoming light and result in depressed signals on the Zodiacal light components. The shapes of the latter are similar to those of normal dispersed spectra (but the signal level is actually depressed in those regions). The IR Blobs are directly visible in the HeI dispersed components as these are generated by nearly monochromatic light at 10830\AA . Note that these HeI Blobs are dispersed images of the Blobs and therefore offset from their positions in broad band imaging

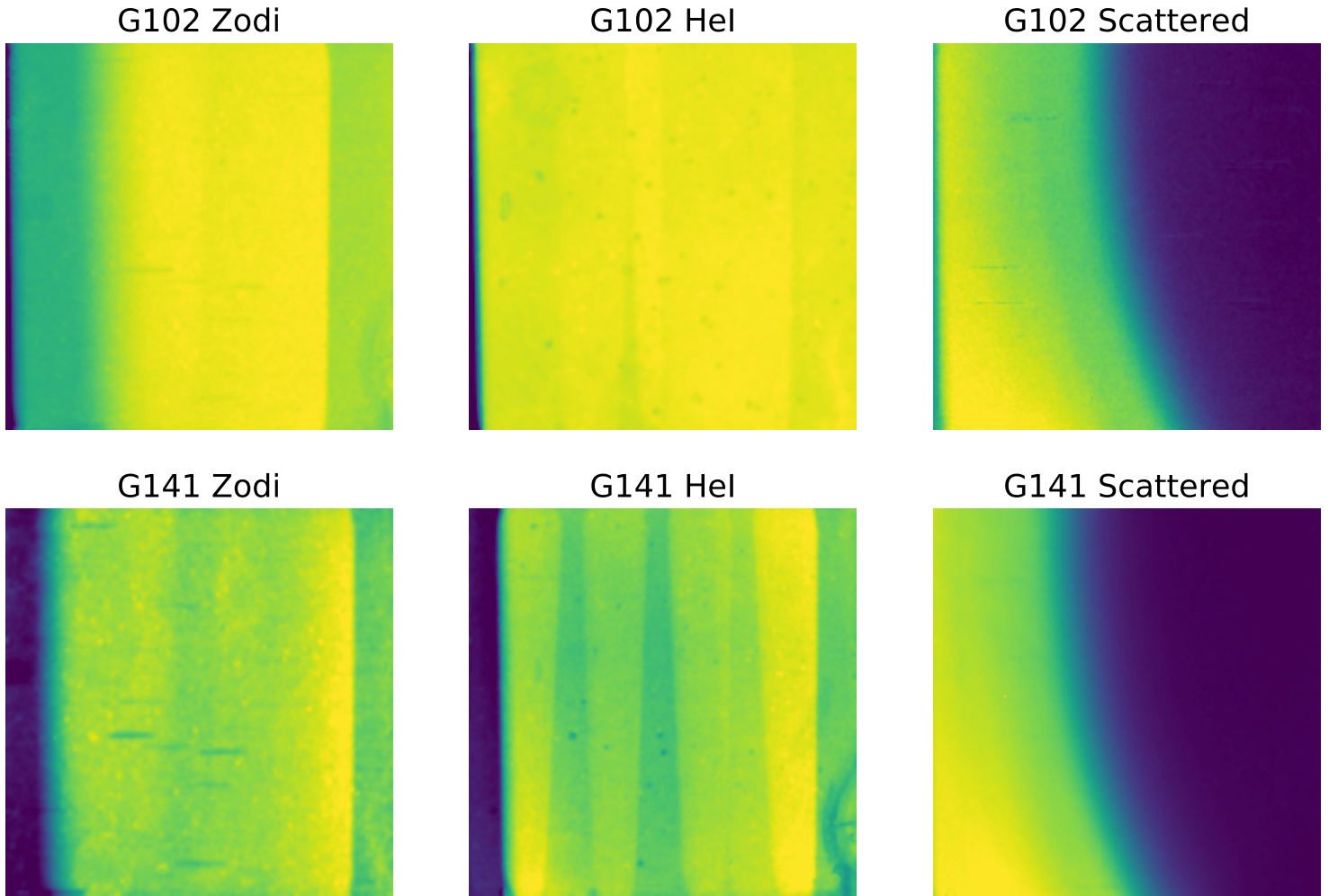


Fig. 10.— Cleaned, "superscrubbed", version of the G102 and G141 background models shown in Figure 9. The elongated features in the Zodi component are caused by the depletion of light from the CSM Blobs. The imprints of the blobs are also visible in the HeI component.

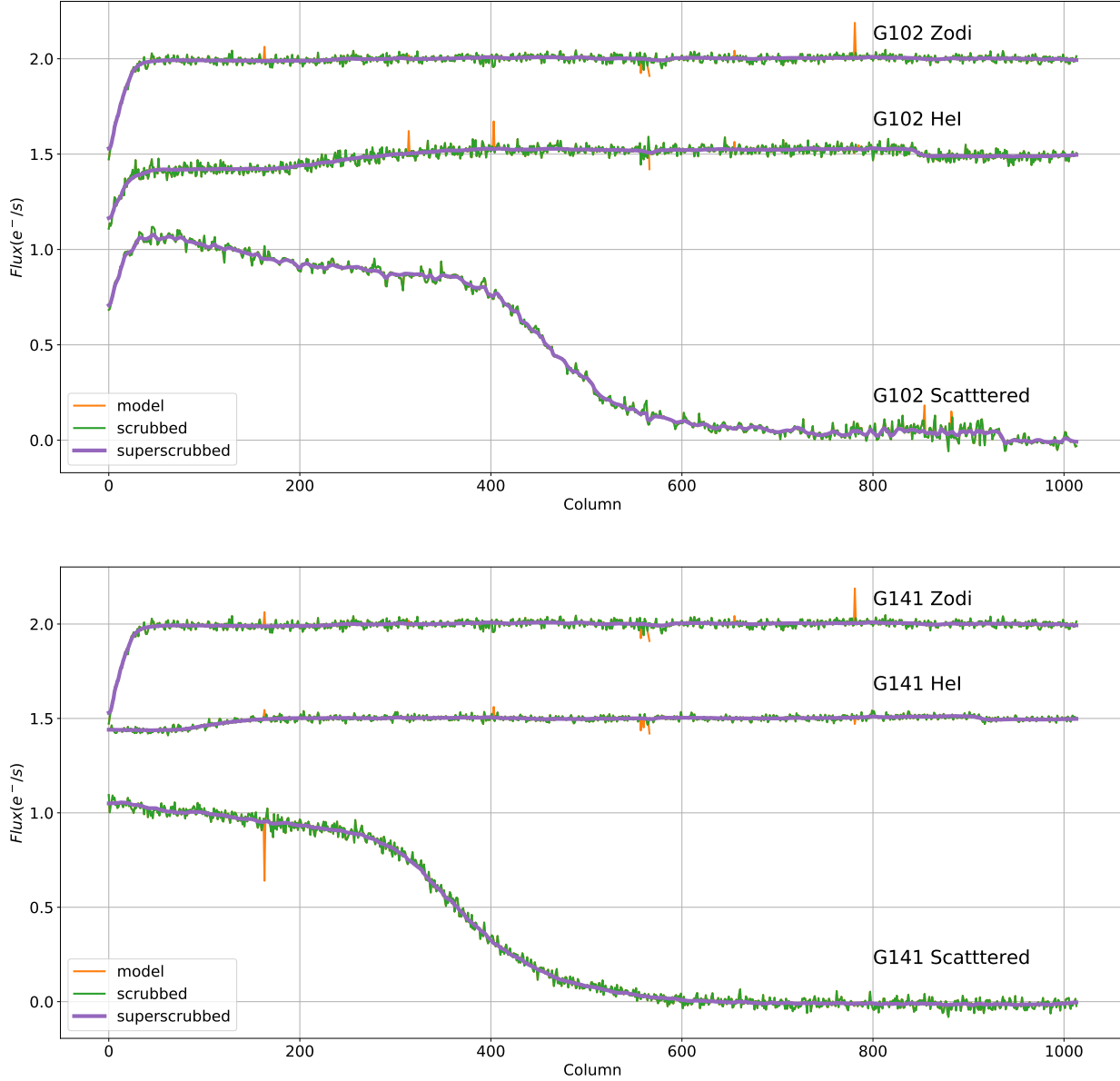


Fig. 11.— Cuts (row 700) of the initial, "scrubbed", and "superscrubbed" versions of the G102 and G141 background models shown in Figure 9. These plots show how the use of ESD allowed the flagging and removal of local spikes in our models and the higher signal to noise of the "superscrubbed" models. Any fitting process is sensitive to local spikes (which are present in the initial version and appear in red here) and both "scrubbed" and "superscrubbed" versions of the models alleviate that problem.

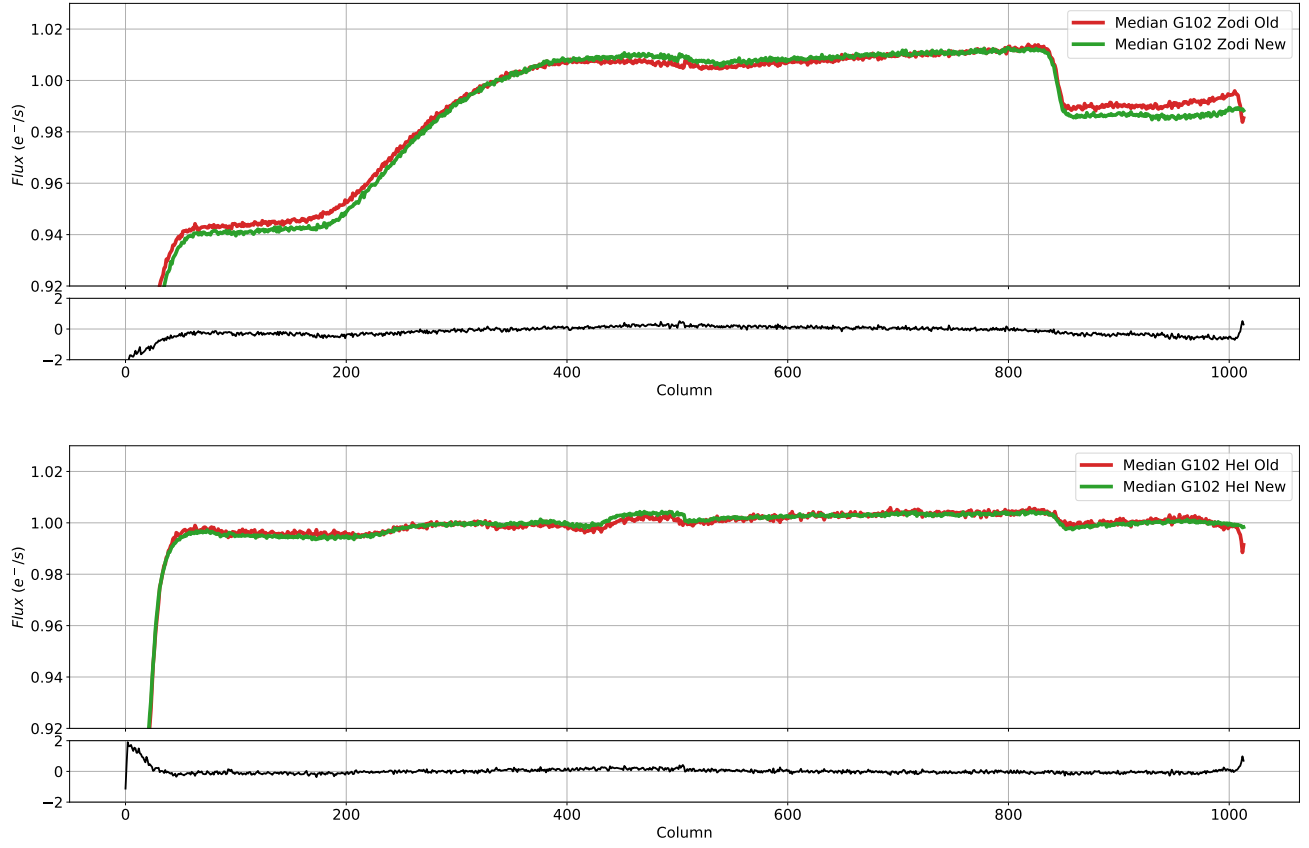


Fig. 12.— The median profile along the row direction of the old and our new G102 Zodi and HeI background models. While they appear similar, they differ most near the edges where as shown in the bottom panel of each plots.

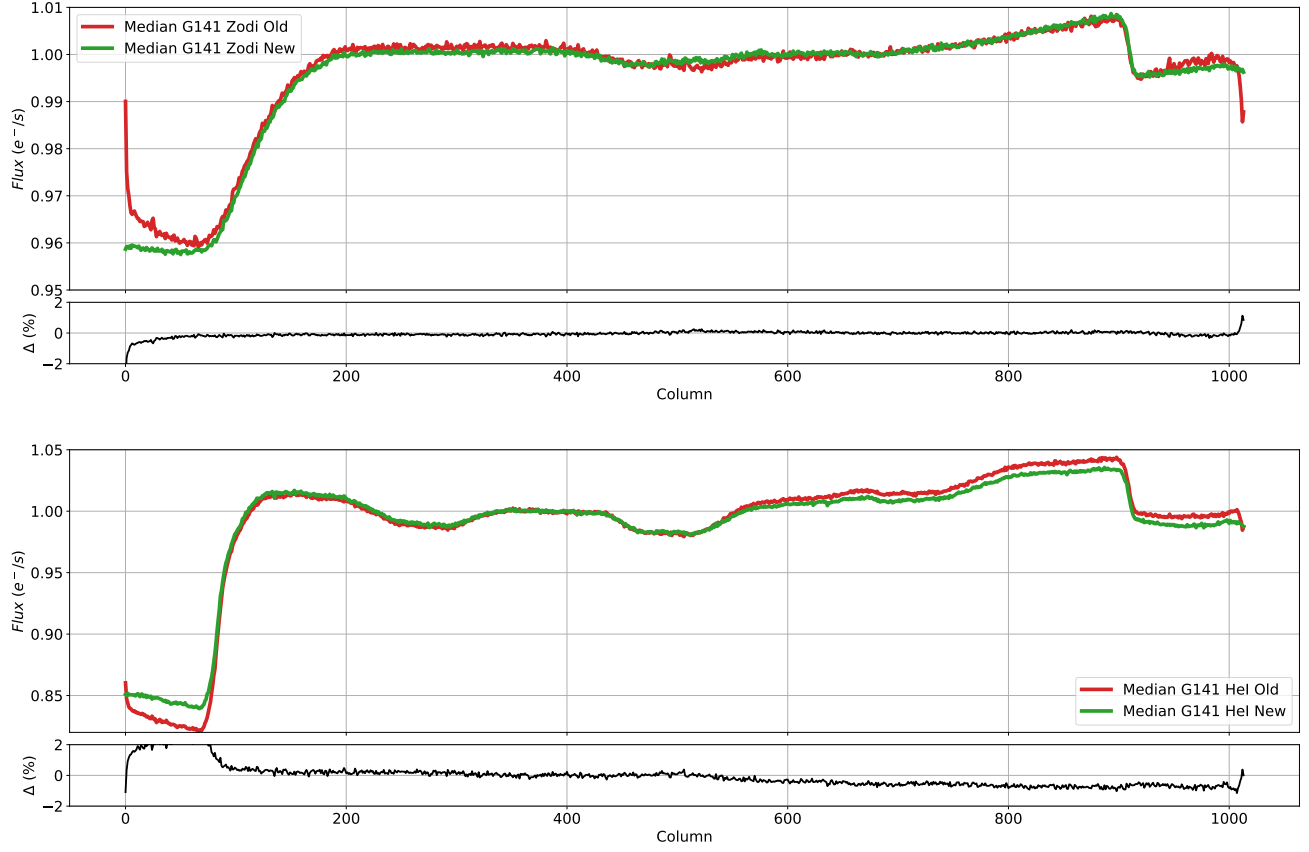


Fig. 13.— The median profile along the row direction of the old and our new G141 Zodi and HeI background models. While they appear similar, they differ most near the edges where as shown in the bottom panel of each plots.

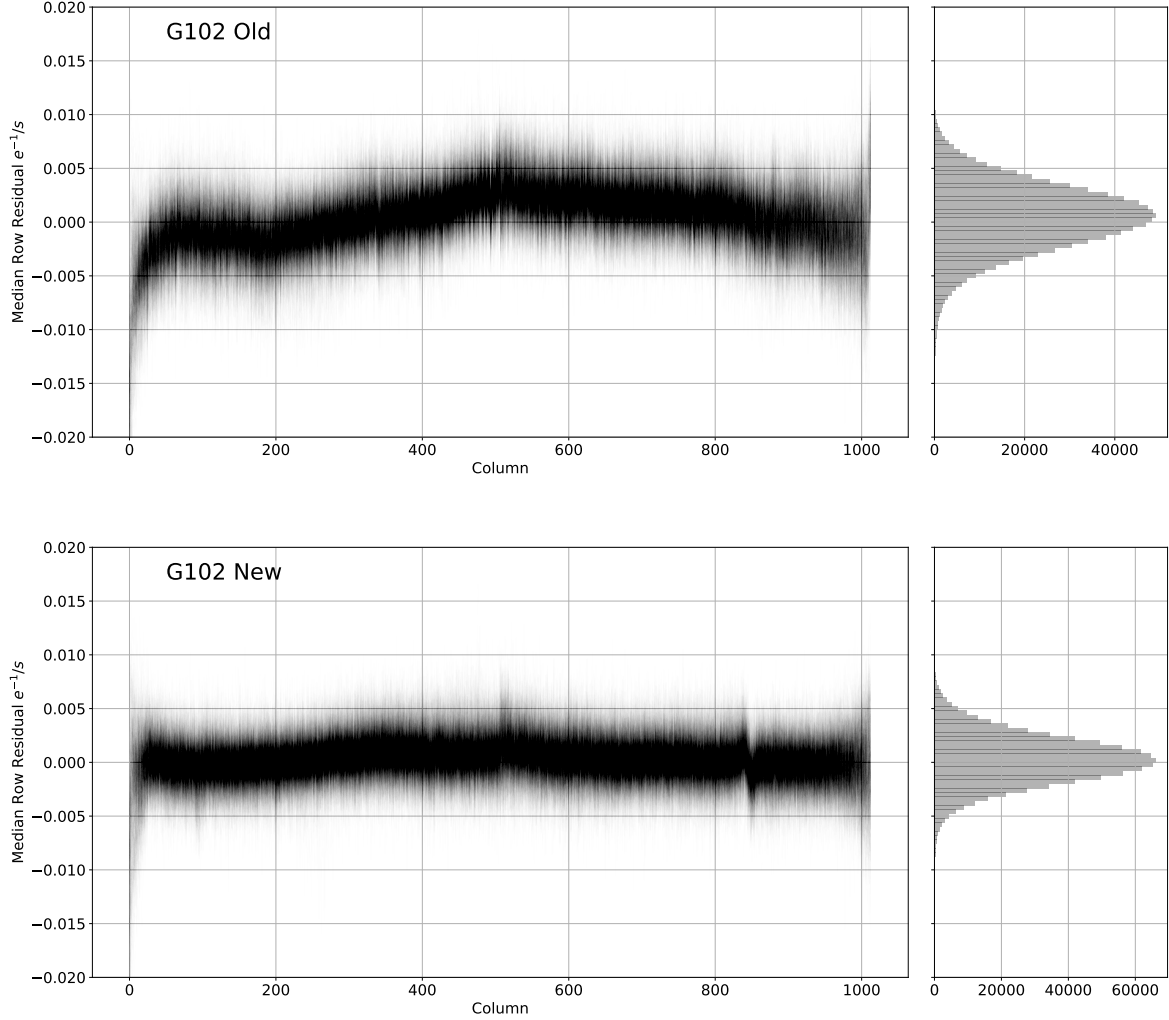


Fig. 14.— We show the residuals to archival G102 datasets when applying the old and new background models. Both plots were generated using the same WFC3 G102 datasets, using the same object masks and same background subtraction technique. We plot the top 40% datasets (894) for which we achieved the lowest overall residuals to illustrate the best results that could be achieved using both the old models and our new models.

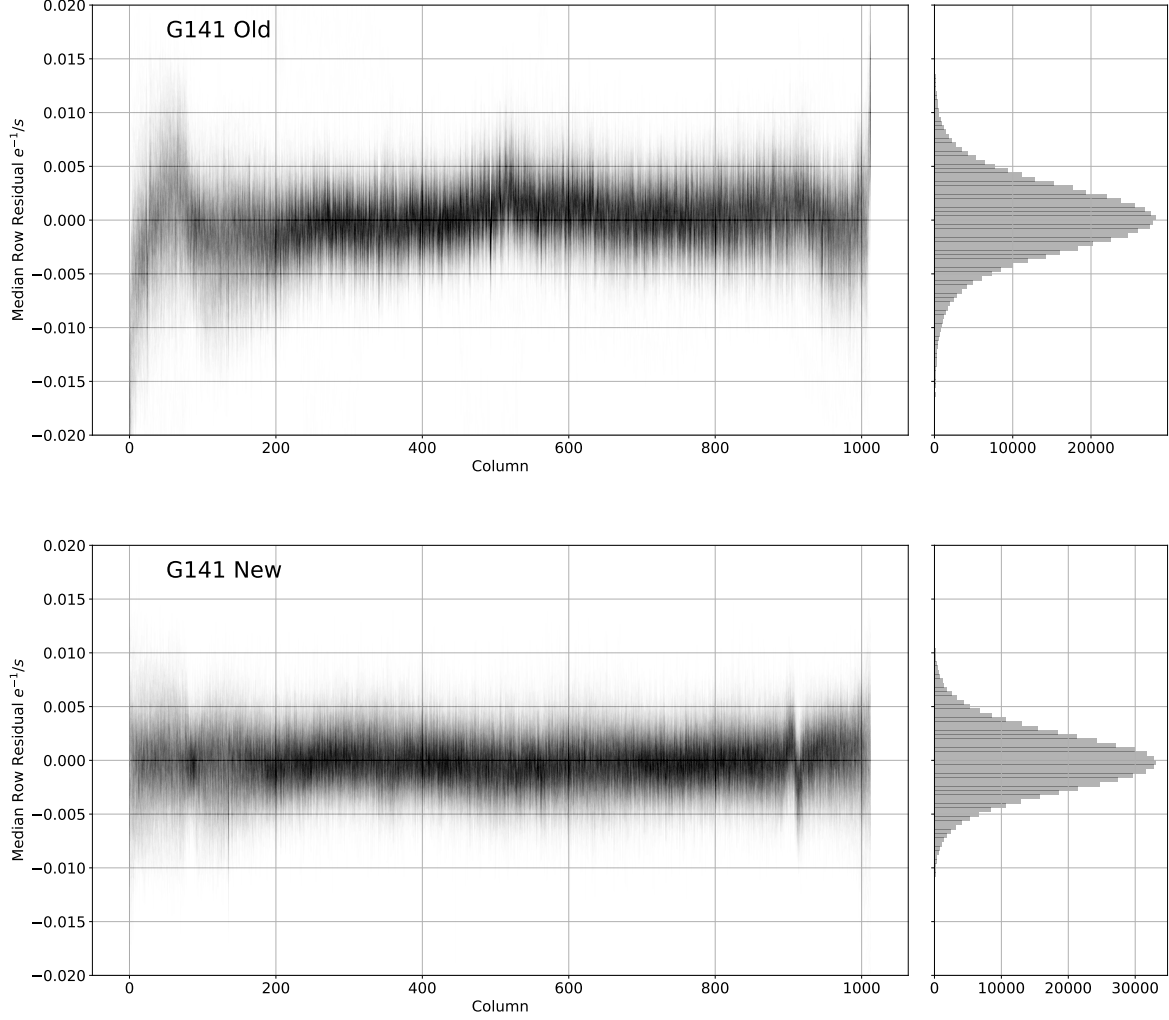


Fig. 15.— We show the residuals of archival G141 datasets when applying the old and new background models. Both plots were generated using the same WFC3 G141 datasets, using the same object masks and same background subtraction technique. We plot the top 40% datasets (553) for which we achieved the lowest overall residuals to illustrate the best results that could be achieved using both the old models and our new models.

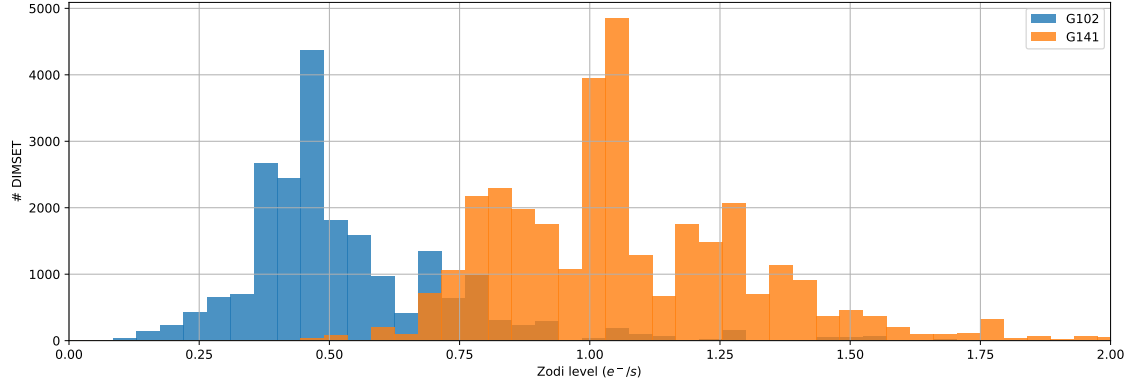


Fig. 16.— The distribution of Zodi levels in WFC3 grism DIMSETs (i.e. individual read)

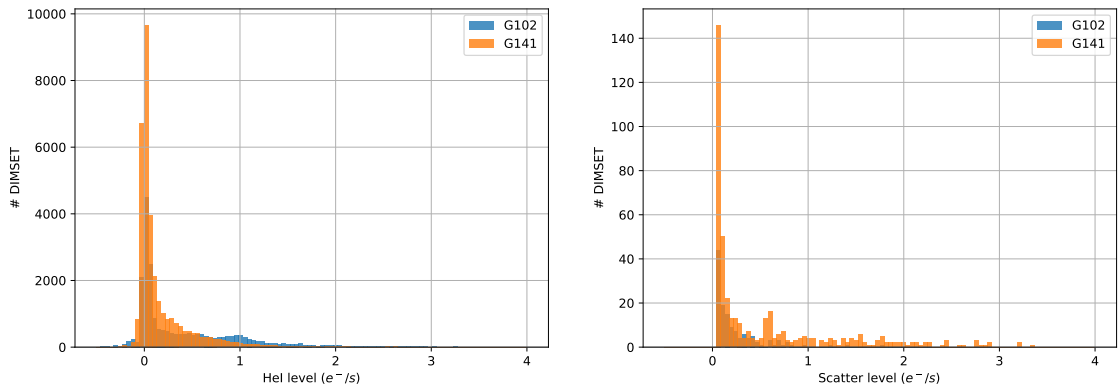


Fig. 17.— Left: The distribution of HeI levels in WFC3 grism DIMSETs (i.e. individual read). Right: The distribution of “Scatter” light levels.

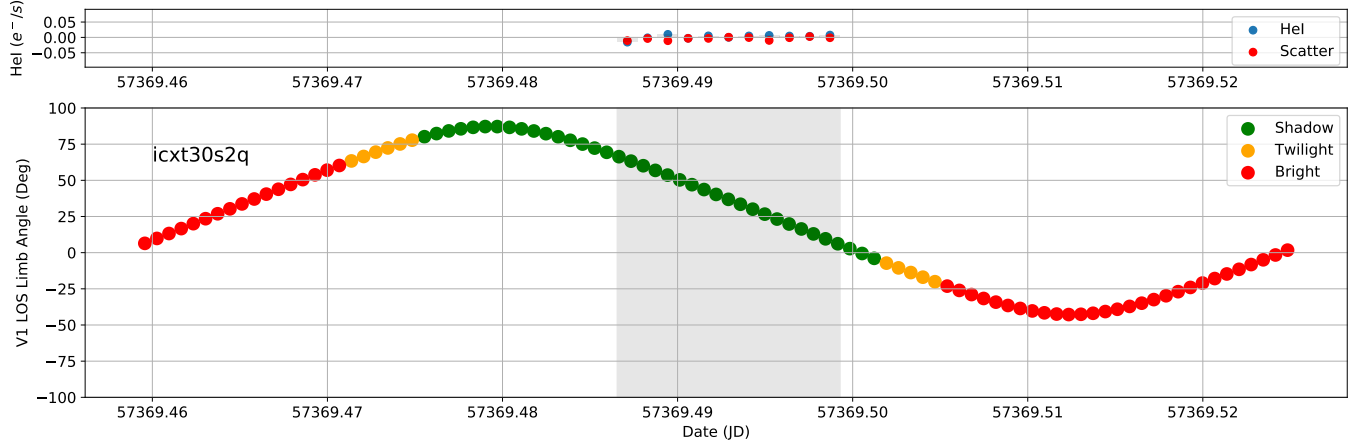


Fig. 18.— Example of an observation with low levels of HeI emission (Top Panel). These data were taken (Bottom Panel, grey shaded area) while the telescope was in the Earth's shadow (Bottom Panel, shown in green)

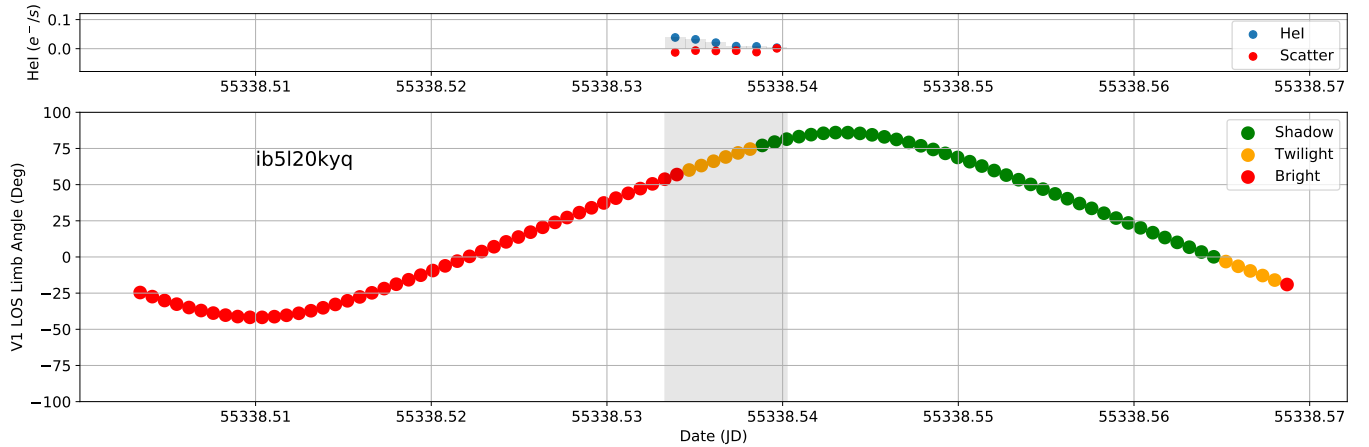


Fig. 19.— Example of an observation with moderate to low levels of HeI emission (Top Panel). These data were taken (Bottom Panel, grey shaded area) while the telescope was moving into the Earth's shadow, with a relatively large Earth limb angle (i.e. looking away from bright Earth limb) but the first reads were affected (Bottom Panel, shown in red, orange, and then green)

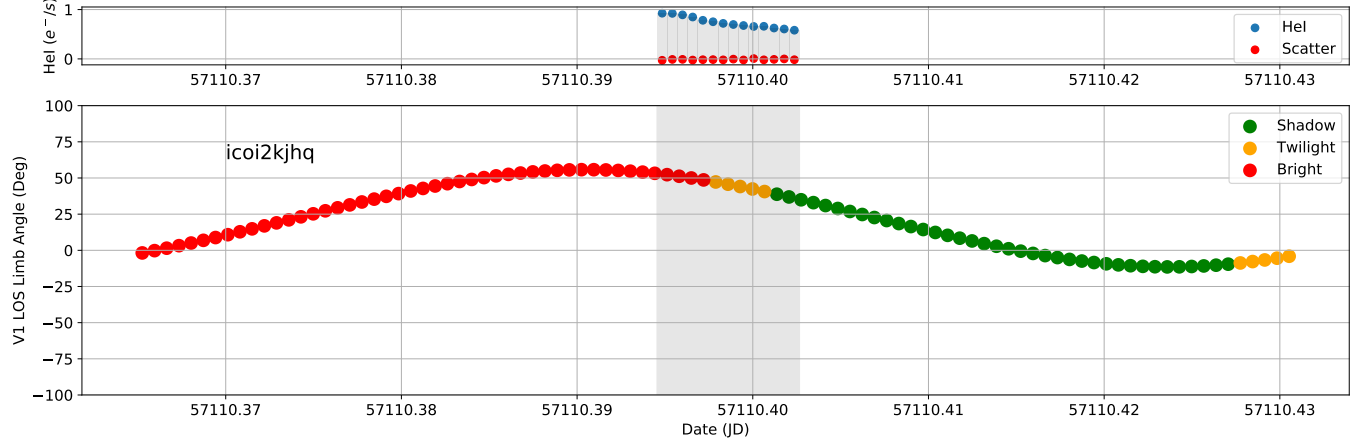


Fig. 20.— Example of an observation with high levels of HeI emission (Top Panel). These data were taken (Bottom Panel, grey shaded area) while the telescope was moving into the Earth’s shadow (Bottom Panel, shown in red, orange, and then green), just as in the case shown in Figure 19 but with a much lower Earth Limb angle (i.e. looking closer to the bright Earth’s limb) and all reads were affected (Top Panel).

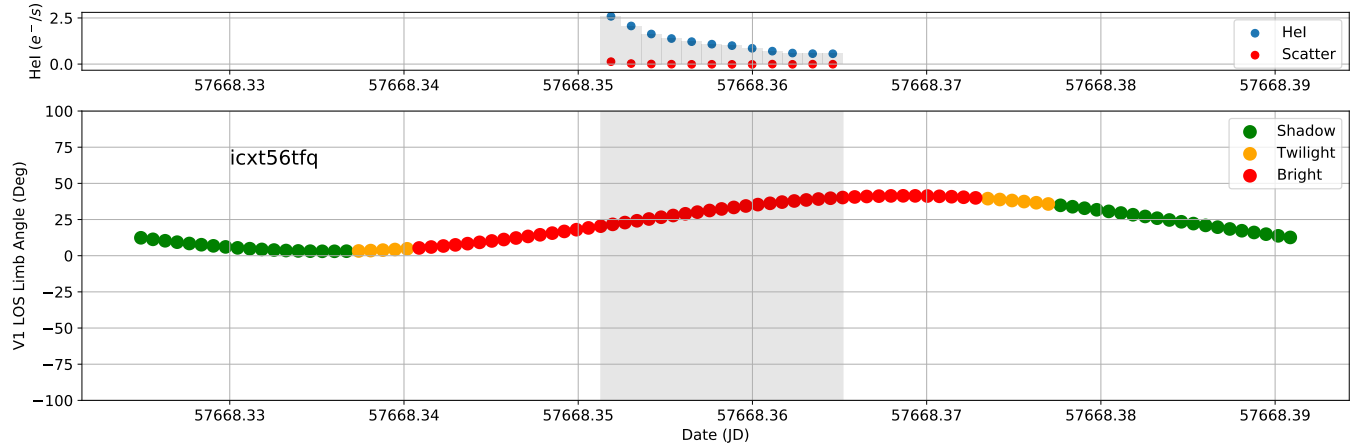


Fig. 21.— Example of an observation with very high levels of HeI emission (Top Panel). These data were taken (Bottom Panel, grey shaded area) while the telescope was not in the Earth’s shadow (Bottom Panel, shown in red,) and with a low Earth Limb angle (i.e. looking closer to the bright Earth’s limb) and all reads were affected (Top Panel). Note how the amount of HeI goes down as the Limb Angle increases and telescope gradually points farther away from the bright Earth limb.

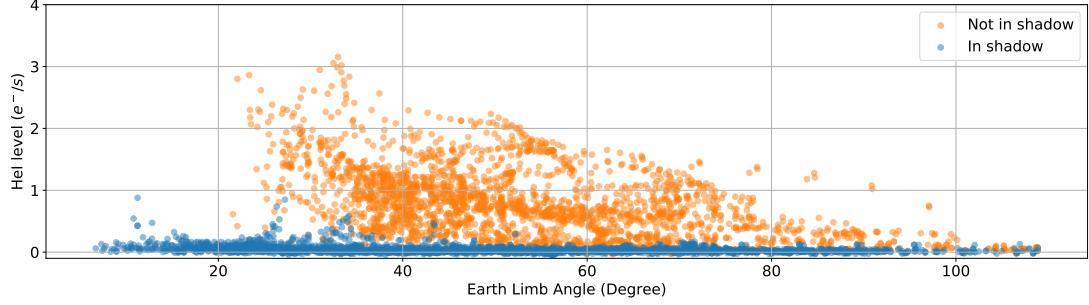


Fig. 22.— The amount of HeI estimates in individual DIMSETs of G102 and G141 datasets, plotted as a function of Earth limb angle. We show DIMSETs taken while in the Earth’s shadow (Blue) and while not in the Earth’ Shadow (Orange). As this plot demonstrates, data taken while in Earth’s shadow remain mostly unaffected. Data taken while looking at the bright Earth limb have an amount of HeI that increases as they are taken at lower Earth limb angles.

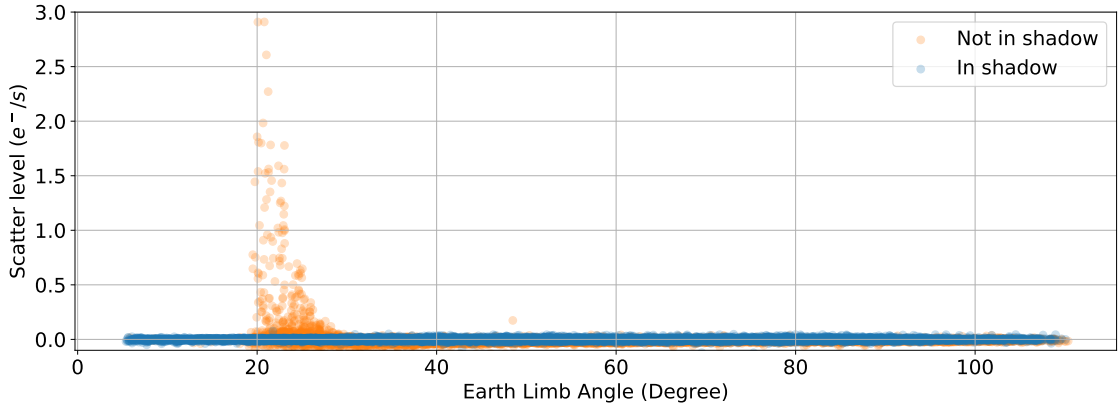


Fig. 23.— Amounts of “scatter” light in individual DIMSETs of G102 and G141 datasets, plotted as a function of Earth limb angle. We show DIMSETs taken while in the Earth’s shadow (Blue) and while not in the Earth’ Shadow (Orange). We detect “scatter” only in observations taken with an Earth limb angle that less than 30 degrees of the bright Earth limb.